Experiments in Fluids (2025) 66:173
https://doi.org/10.1007/s00348-025-04098-7

RESEARCH ARTICLE

On the interaction of a linear plug nozzle flow with sub-, trans-, and supersonic outer flow

Paul Wißmann[1] · **Christian J. Kähler**[1] · **Sven Scharnowski**[1]

Received: 27 January 2025 / Revised: 3 June 2025 / Accepted: 1 August 2025 / Published online: 31 August 2025
© The Author(s) 2025

Abstract

A plug/aerospike nozzle is a promising concept as a propulsion system for space launchers and space planes. The inherent ability to adapt the nozzle jet to the ambient pressure level improves the thrust performance under overexpanded operating conditions compared to conventional bell nozzles, which is of great interest for future single-stage-to-orbit vehicles. This experimental study investigates the topology and aerodynamics of a cold flow linear plug nozzle jet in an outer flow environment. PIV and high-speed schlieren measurements are utilized to understand the mutual aerodynamic interaction between each other. The jet flow is studied for a variety of nozzle pressure ratios in combination with an outer flow at sub-, trans-, and supersonic Mach numbers. The flow is examined for two plug lengths, which are 72% and 24% of an ideal contour. It is found that the combination of nozzle pressure ratio and outer Mach number strongly influences the flow pattern and local velocity magnitudes. Backflow regions are measured, mainly emerging through the integration of the nozzle in a bluff aft body. The strength and frequency of aerodynamic modes are found to be highly dependent on the operating conditions as well. The most relevant ones are jet screeching, alternating vortex shedding of the outer flow, and vortex shedding in the base wake of the plug with strong truncation. The latter causes strong fluctuations in the flow, which are transmitted to the shear layer and induce acoustic wave emission. In addition, the flow locally accelerating in the plug base region results in increased shock strength in the jet structure. At trans- and supersonic outer flow, however, the aerodynamic modes of the jet flow are strongly suppressed. The impact of plug truncation on the velocity field becomes less for higher nozzle pressure ratios and outer flow Mach numbers.

1 Introduction to plug nozzles

In modern space launch vehicles, the aft section incorporates bell nozzles, which are essential for thrust generation. In an optimal design scenario, the expanded flow adheres to the bell contour, and the velocity vectors at the nozzle outlet are aligned parallel to the direction of flight. Any deviations from this ideal condition (e.g. due to ambient pressure variations during the ascent) result in a reduction in effective thrust, as the radial components of the thrust vectors from the supersonic jet do not contribute to the vehicle's acceleration. In this case, the nozzle pressure ratio *NPR* defined as

$$NPR := \frac{\text{Total nozzle pressure}}{\text{Static ambient pressure}} = \frac{p_{0,\mathrm{n}}}{p_\infty} \tag{1}$$

differs from the design pressure ratio NPR_D given by the specific shape of the nozzle's inner contour. Especially when the nozzle is operated in extremely overexpanded conditions, namely when the *NPR* is much lower than NPR_D (altitudes proximate to sea level), there is an elevated risk of flow separation along the nozzle's inner surface. Any unsteady and asymmetric separation scenarios can lead to dangerous lateral forces, or side loads, which drastically increase the probability of structural failure (Nave and Coffey 1973). Among the various loss mechanisms related to the combustion or non-uniformity of the exiting flow, the non-ideal expansion of the propellants and an inhomogeneous exit flow (divergence losses) are by far the most significant (Manski and Hagemann 1996; Hagemann et al. 1998).

✉ Paul Wißmann
paul.wissmann@unibw.de

Christian J. Kähler
christian.kaehler@unibw.de

Sven Scharnowski
sven.scharnowski@unibw.de

[1] Institute of Fluid Mechanics and Aerodynamics, University of the Bundeswehr Munich, Werner-Heisenberg-Weg 39, Neubiberg 85577, Bavaria, Germany

When the design principle is inverted in a manner that the exhaust jet is guided by an inner contour forming a spike/plug (see Fig. 1), the aforementioned limitations can be addressed and effectively mitigated (Arnold 1954; Ruf and McConaughey 1997; Nasuti and Onofri 2001; Onofri et al. 2002). The development of aerospike or plug nozzle technology has spanned several decades, beginning with early proposals in the 1950s as a means to achieve altitude-compensating thrust for more efficient rocket propulsion. The initial concept of a plug nozzle, also referred to as an aerospike nozzle, was proposed by Arnold (1954) in 1954. By the 1960s and 70s, hot-fire ground tests began validating the aerospike's potential of elevated thrust performance, although technical challenges like cooling, throat erosion, and structural complexity limited full-scale adoption (Burry et al. 1967). Interest resurged in the 1990s and early 2000s with programs like the Lockheed Martin X-33, which, among others, included extensive hot-fire tests of linear aerospike engines (D'Agostino et al. 2001; Besnard et al. 2002; Bui et al. 2005). Although the X-33 never flew, these efforts advanced fabrication techniques and deepened understanding of flow separation, base drag, and plume behavior. Later research has included rare but critical supersonic flight tests that provided in-situ performance data (Corda et al. 1998). Advances in computational fluid dynamics and experimental diagnostics have also improved the investigation of complex aerodynamic phenomena in more detail in a controlled measurement environment. Together, these efforts have matured the technology, though integration and flight-readiness remain areas of ongoing development.

The nozzle geometry is the decisive feature that ultimately results in aerodynamic and performance-related advantages. In the overexpanded case the nozzle jet is guided by the contour of the inner plug. By this, a system of expansion and compression waves generates a parallel exhaust jet, while substantially reducing the risk of failure due to flow separation on the inner surface. Hence, within the overexpanded regime, the aerospike nozzle demonstrates enhanced thrust coefficient performance relative to traditional bell nozzles. The exhaust jet is capable of adapting continuously to the prevailing ambient pressure. This is of particular importance for future single-stage-to-orbit (SSTO) rockets and space planes. Especially for the latter ones, the geometry of a linear aerospike nozzle facilitates a more effective nozzle integration into the aft section of the vehicle and optimizes the utilization of the base area, while allowing thrust vector control strategies. The design inherently supports high area ratios. In underexpanded conditions, the nozzle performance approaches that of bell-shaped nozzles.

An understanding of the flow of the exhaust jet is of fundamental importance. However, to gain a more realistic perspective, it is also necessary to consider the in-flight nozzle performance. The mutual interaction between the nozzle's jet flow and an outer flow at certain Mach number Ma_∞ has been already shown experimentally for generic bell and dual-bell nozzle concepts (Scharnowski et al. 2016; Scharnowski and Kähler 2021), where the mean reattachment length of the outer flow, the shock strengths and the dual-bell nozzle mode depend on the combination of free-stream Mach number and *NPR*. In this study, a linear aerospike nozzle flow is investigated with the ability to vary these operation parameters independently in a controlled wind tunnel setting.

A simplified schematic of the flow pattern of a plug nozzle jet operated at design conditions with presence of an arbitrary outer flow is shown in Fig. 1. Shear layers are indicated in gray. Nozzle and outer flow are highlighted in green and yellow, respectively, with the black vectors representing the local flow direction. The two green dotted lines above and below the plug represent the last expansion Mach lines (design characteristic), after which the nozzle flow is in an ideal case perfectly horizontal. A more detailed and realistic view is presented in Fig. 2, where an overexpanded nozzle flow in combination with a supersonic outer flow is shown. Flow expansion and compression effects are denoted in blue and red, respectively. Slip lines are shown as purple dashed

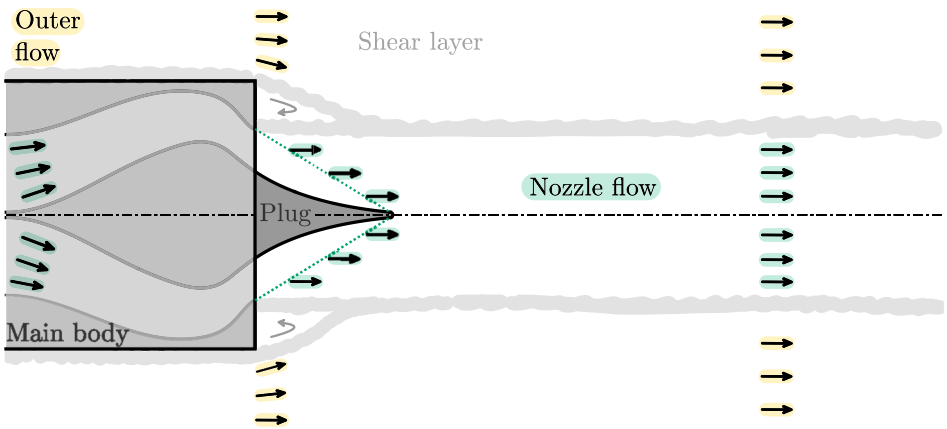


Fig. 1 Simplified schematic of a plug nozzle jet under ideal design conditions. The nozzle flow (green), outer flow (yellow), and shear layer (gray) are indicated, while the arrows outline the flow direction

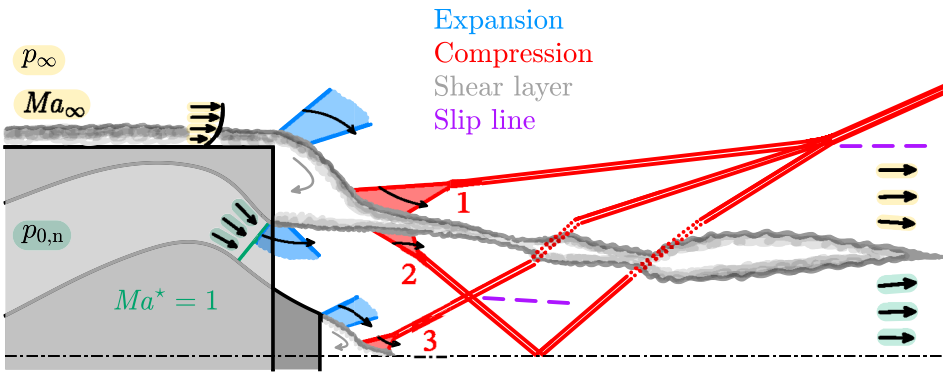


Fig. 2 Detailed schematic flow topology of a truncated plug nozzle jet in combination with supersonic outer flow. Flow expansion (blue), compression (red), and slip lines (purple) are indicated. Compression waves merge to form oblique shocks, namely the outer realignment shock (1), inner realignment shock (2), and the trailing shock (3)

lines. The extent of the expansion waves and the length of the slip lines are chosen arbitrarily. Note, that a highly relevant adaptation to the plug is introduced, which is to cut the spike's tip. It is well known that the tip does not contribute much to the generated thrust (Ruf and McConaughey 1997; Wisse and Bannink 2001), produces additional weight, and that it is a major challenge to cool the thin material when the nozzle is operated with a hot exhaust gas. However, this intentional truncation comes with its aerodynamic implications, as indicated in the schematic.

In the nozzle chamber of the main body the flow accelerates toward the outlets. After reaching sonic conditions in the nozzle throat ($Ma^\star = 1$), the flow starts to expand at the nozzle lip until the ambient pressure and the pressure in the nozzle jet are equal. As the flow pattern in an overexpanded case (Fig. 2) progresses downstream, a system of expansion and compression regions emerges, with the latter tending to merge to form oblique shocks. The ones emerging from the outer and inner shear layers are referred to as outer (1) and inner (2) realignment shocks. The one originating from behind the plug base is called trailing shock (3). Shock-shock interactions lead to slip conditions. The shocks interacting with the shear layer leads to a sudden thickening. However, the interaction is complex and not fully understood, which is why the shocks passing through are only indicated with dotted lines. In the far field, the outer realignment shock, the trailing shock, and the inner realignment shock from the bottom half merge to form a single shock wave. At sub- and transonic flight conditions it will be apparent that the overall flow pattern is different, with an absence of the realignment shocks.

2 Research objectives

The paper aims to characterize the sensitivity of a plug nozzle's flow field and its performance with respect to the outer flow conditions. The interaction between nozzle jet and outer flow across diverse flight regimes is complex and important to investigate in detail because the flow in each regime has distinct characteristics in terms of shock waves, boundary layer behavior, and potential flow separation. Research in this field is crucial for the development of propulsion systems for future space launchers and hypersonic vehicles. Especially the aerodynamic implications of various flow scenarios are not yet understood and ask for further studies.

The steady-state flow topology and shock pattern of a plug nozzle jet are fairly well researched through numerical (Immich et al. 1998; Wisse and Bannink 2003; Geron et al. 2005) and schlieren imaging studies (Tomita et al. 1996; Immich et al. 1998; Hagemann et al. 1998; Wisse and Bannink 2001; Verma 2009). In-flight conditions, i.e. the effects of an outer free stream, have been studied in many numerical studies, but experimental investigations are rare (Wisse and Bannink 2001; Chutkey et al. 2018). Quantitative measurements through particle image velocimetry (PIV) (Tobias and Agrawal 2023) and research on high-speed dynamics and aeroacoustics of the jet plume (Karthikeyan et al. 2009; Powis et al. 2016; Zaman et al. 2022; Golliard and Mihaescu 2024; Zaman et al. 2024; Bharathwaj et al. 2024) for a plug nozzle specifically are rare too, and the physics is not well understood. Measurements with a truncated plug have been performed in many of the existing publications, but a standardized plug length definition is hard to find. In addition, a plug with a simple conical shape is often used instead of a properly designed plug contour according to the method of characteristics (Angelino 1964). Studying a wide range of both NPR and Ma_∞ experimentally hasn't been done in such extent and can provide a more holistic understanding of the jet aerodynamics at various flight regimes. For that, multiple combinations of nozzle and outer flow conditions are realized, while comparing the flow for two different plug lengths (72 % and 24 % of an ideal contour). The following research questions are to be addressed within the scope of this work:

- How is the velocity field and flow pattern of two different plug lengths at various *NPR*s influenced by an outer flow in the sub-, trans-, and supersonic regime?
- How do the nozzle jet and outer flow aerodynamics (periodic phenomena) behave when facilitating a sub-, trans-, and supersonic outer flow and varying the applied *NPR*?

This work follows up on the work by Wißmann et al. (2025), where the plug nozzle flow is studied in detail for a multitude of *NPR*s without consideration of an outer flow. Preliminary results about the interaction between nozzle and outer flow for one specific $NPR \approx 4.5$ can be found in Wißmann et al. (2024).

This paper is structured in the following way: After an introduction to the experimental facility and the measurement methods, the outer flow dynamics are characterized using schlieren recordings. Decoupling the nozzle and the outer flow investigation before delving into the combined flow is intended to provide the foundation for understanding the behavior of the nozzle jet in external flow scenarios. Afterward, the nozzle jet in interaction with the outer flow is investigated, where PIV results in two different planes and time-resolved high-speed schlieren results are presented and analyzed. The findings are summarized in a last section, where concluding remarks finish up the paper.

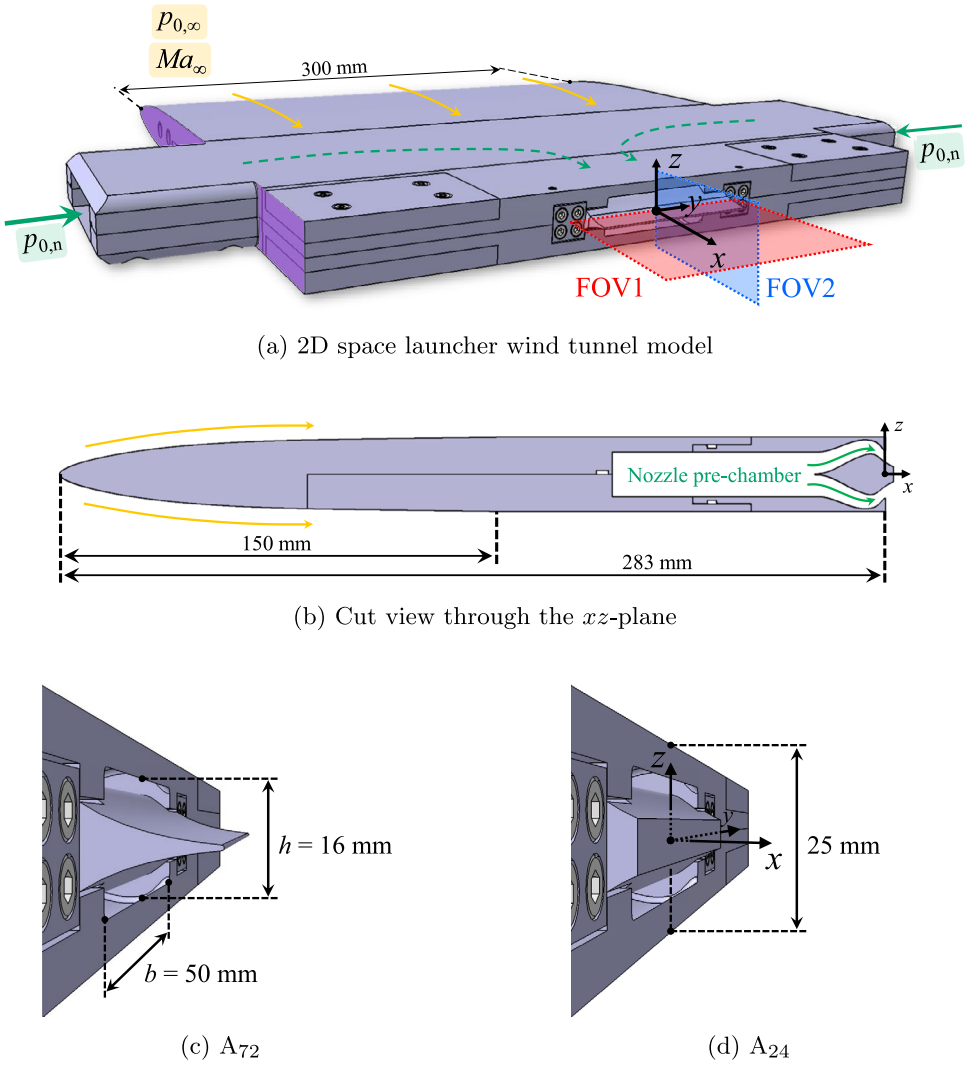
3 Test facility and measurement methods

For answering the research questions stated above, wind tunnel experiments are performed in the Trisonic Wind tunnel Munich (TWM) at the University of the Bundeswehr Munich. The TWM is a blow-down wind tunnel with Mach numbers encompassing the subsonic, transonic, and supersonic regime. 43 holding tanks with a total volume of approximately 350 m^3 can be filled with dry air at up to 20 bar and serve as a pressure reservoir. A pressure control valve adjusts the total pressure $p_{0,\infty}$ in the test section between 1.2 bar and 5 bar. Two adjustable throats, one upstream (Laval nozzle) and one downstream (diffuser) of the measurement section, allow a continuous Mach number range from 0.3 to 3.0 in the test section. The test section measures 675 mm in height and 300 mm in width upstream of the model and measurement location. The height steadily increases symmetrically toward 700 mm downstream of the model to compensate for the growing displacement thickness. During the runtime the static pressure is measured in the floor and the ceiling at several points within test section along the streamwise direction. The local Mach number is determined based on the ratio of the locally measured static pressure and the total pressure. The reference Mach number shown in the subsequent schlieren and PIV results plots is the inflow Mach number Ma_∞ determined at a location on the ceiling approximately 439 mm upstream of the model's leading edge. The effective runtime is in-between 30 s and 240 s in the viable $p_{0,\infty}$ and Ma_∞ range. The free-stream turbulence level, being assessed by analyzing streamwise velocity fluctuations, is 1.9 % at a Mach number of 0.3. This turbulence level decreases as the Mach number increases, reaching 0.45 % at $Ma_\infty = 3.0$ (Scharnowski et al. 2019).

The wind tunnel flow represents the outer flow around a generic 2D space launcher model, as shown in Fig. 3a) (yellow). The model is placed in the center of the test section with respect to z. It has a thickness of 25 mm and a width in y-direction that is equal to the wind tunnel's test section width (300 mm), ensuring a tight fit within the wind tunnel side walls. The side walls face against the surfaces highlighted in purple in Fig. 3afrom both sides of the model. This means that the protruding nozzle pressure inlets (green) are located outside the wind tunnel test section, not surrounded by the outer flow. For the nozzle flow realization, two pressure hoses (one on each side) connect the nozzle pre-chamber to the holding tank system. The pre-chamber guides the flow and combines it before the nozzle throats (green arrows). The forebody geometry of the leading edge features a nose of 150 mm length followed by a flat main body. The aft section of the 2D space launcher model contains the linear plug nozzle. The total external body length adds up to 283 mm (see Fig. 3b). The nose contour and the smooth transition to the aft section has been designed to ensure a shock-free flow up to $Ma_\infty = 0.8$. However, in supersonic inflow conditions, the bluff nose of the model induces oblique shocks propagating toward the test section ceiling and floor. Those slightly reduce the local Mach number further downstream above and below the model, respectively. For further reading about the forebody geometry and how it effects the wind tunnel flow it is referred to Bolgar et al. (2018). This linear model, in contrast to an axisymmetric one, is well suited for the given wind tunnel configuration and simplifies the experiments by minimizing 3D effects. Moreover, it represents a realistic design approach when it comes to aerodynamically shaped SSTO space planes.

The design of the nozzle's plug contour was based on the method proposed by Angelino (1964), with a design Mach number of $Ma_D = 2.5$, resulting in a design nozzle pressure ratio of $NPR_D \approx 17.1$. Fig. 3c and d present a detailed view of the nozzle throat for two manufactured plugs of varying lengths. These configurations are henceforth designated as A_{72} and A_{24}, representing the 72 % and 24 % truncated plug, respectively.[1] The nozzle exit height and width are

[1] A 100 % plug would include all theoretically determined contour points according to the method by Angelino (1964) and would represent the theoretical optimum from an aerodynamic standpoint. The manufactured plug has a 0.25 mm radius at the spike for construction reasons. Consequently, the plug is shorter and only contains a fraction of the calculated ideal contour points. The length definition is based



(a) 2D space launcher wind tunnel model

(b) Cut view through the xz-plane

(c) A_{72}

(d) A_{24}

Fig. 3 Schematic of the wind tunnel model featuring a nozzle throat with interchangeable plug types

Table 1 Outer flow schlieren measurement parameters

FOV size (x/z) in px	1024/352
Scaling in px/mm	12.47
Exposure time in µs	15
Sampling frequency in kHz	61.8
Number of images recorded	10^4

denoted as $h = 16$ mm and $b = 50$ mm, respectively. For more details about the nozzle design it is referred to Wißmann et al. (2025).

Footnote 1 (continued)

on the plug's contour projected onto the x-axis, starting from the nozzle throat where the sonic condition is reached and the flow begins to expand. According to that, the long plug has a length of about 72 % compared to the theoretical optimum. The plug with the extra intentional truncation only features about 24 % of the length of the ideal contour and is named accordingly.

PIV measurements with 10.5 Hz are performed in two field of views (FOVs) from different viewpoints. FOV1 represents the xy-plane (top view) and FOV2 the xz-plane (side view), as indicated in Fig. 3a in red and blue, respectively. Note that the measurement plane for FOV1 is chosen to be at $z \lesssim 0$ mm, meaning at the models center but slightly shifted down towards negative z. This was done to avoid severe light reflections at the A_{72} spike's tip. For FOV2, the xz-plane is illuminated by a light sheet entering from downstream at $z \approx 0$ mm. This enables measurements slightly inside the nozzle throats and a simultaneous visualization of the top and bottom halves of the nozzle and outer flow. A Nd:YAG double pulse laser of the SpitLight Compact 400-10 type by InnoLas Laser GmbH with a pulse width of four to eight nanoseconds is used to generate the light sheet. The flow is seeded by Di-Ethyl-Hexyl-Sebacat (DEHS) particles with a particle response time of approximately 2 µs (Ragni et al. 2011) and a mean diameter smaller than 1 µm (Raffel et al. 2018). Particles were fed into the outer flow upstream the

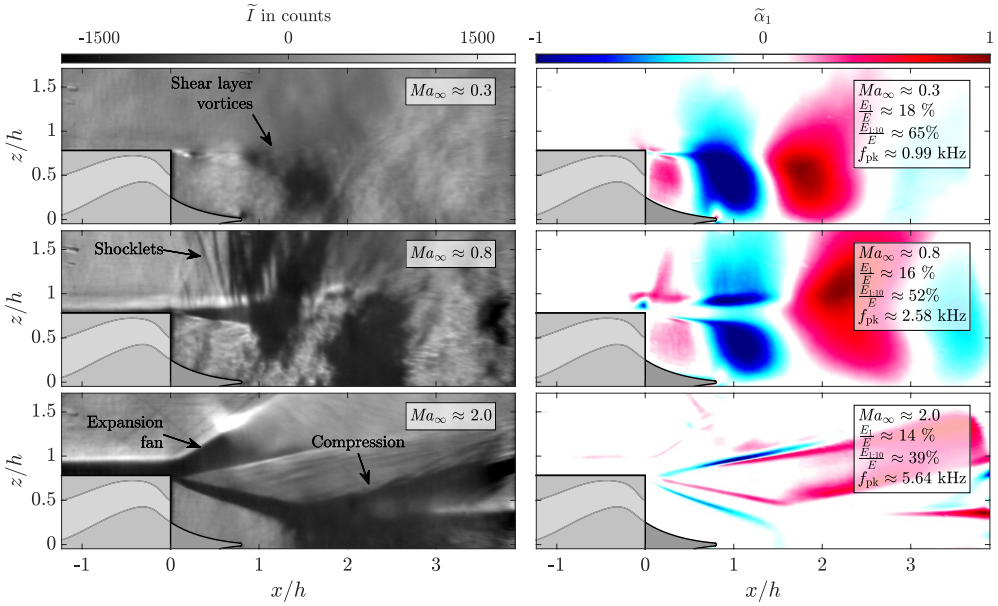


Fig. 4 Outer flow schlieren measurements and most dominant POD modes

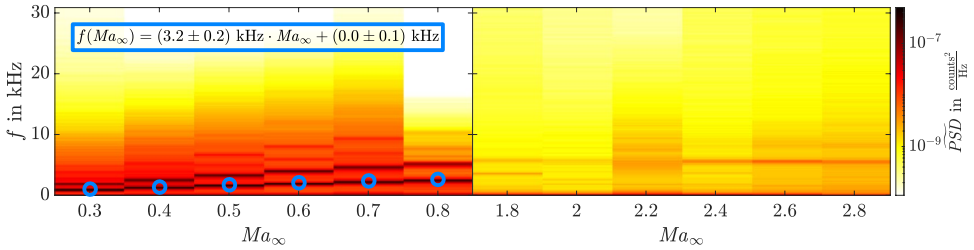


Fig. 5 Outer flow POD-based spectrogram

settling chamber. Independently, another seeding generator feds the particles into the nozzle flow far upstream the nozzle throats. The image pairs are recorded using an Imager sCMOS camera from LaVision GmbH. Exemplary raw particle images for FOV1 and FOV2 are provided in the supplementary material.

The velocity field measurements are complemented by high-speed schlieren recordings from the side view. After the collimated LED light has passed through the test section, it is focused onto a vertically (z-axis) oriented knife edge, which translates the local streamwise density gradient in the flow into light intensity. The signal is captured by a Phantom v2640 high-speed camera by Vision Research Inc. As the linear plug nozzle is symmetric with respect to the xy-plane, some recordings are made of the upper nozzle half only. By this, a smaller fraction of the sensor area is used, making an increase in the frame rate up to 100 kHz possible. This allows to temporally resolve high frequency flow features.

4 Characterization of the outer flow

At first, schlieren measurements of only the outer flow are carried out at free-stream Mach numbers Ma_∞ in the range between 0.3 and 0.8 for the sub-/transonic regime and between 1.8 and 2.8 for the supersonic regime in 0.1 steps, respectively. The intention here is to characterize the outer flow dynamics and decouple them from the nozzle flow itself, before investigating the combination of both. The measurement parameters are summarized in Table 1.

Figure 4 contains exemplary schlieren snapshots of selected Ma_∞ in the left column, where the first row is representative for the sub-, the second row for the trans-, and the third row for the supersonic regime. Hereby, $\widetilde{I}$ is the measured schlieren intensity minus the intensity recorded at still air. The most energetic proper orthogonal decomposition (POD) (Zigunov 2024) mode is shown in the right column. The normalized mode intensity $\widetilde{\alpha}_i$ is color scaled, where i stands for the mode index. E_i therefore is the energy content of mode i. E is the total energy of all modes, i.e. the whole flow field. The fully captured range of Ma_∞ is accounted for in the spectrograms in

Fig. 5, emphasizing how dominant frequencies in the flow field change with Ma_∞. Each power spectrum is computed from the temporal evolution of the mode intensities using Welch's method (Welch 1967). Hereby, the average of the POD modes spectra is computed, where each spectrum is weighted according to the corresponding POD mode's energy contribution. Hence, the color scale shows the energy weighted average power spectral density estimate $\widetilde{PSD}$:

$$\widetilde{PSD} = \sum_i \frac{E_i}{E} \cdot PSD_i \,. \tag{2}$$

For the spectra, only the ten modes with the highest energy contribution ($i = 1 \ldots 10$) are accounted for, as they already contain a significant proportion of the total energy and the remaining modes would mostly add noise. The most prominent peak frequency in the average spectra is denoted as f_{pk}. All outer flow measurements are executed with the A_{72} plug, and they are assumed to be representative for the plug with truncation as well.

In the sub- and transonic regime (first and second rows of Fig. 4) the flow is dominated by a periodic asymmetric vortex shedding mode. As shown in the first POD modes, the structures grow spatially in downstream direction. This has already been shown for a backward-facing step flow of the same forebody model by Scharnowski et al. (2017). The fundamental frequency (Fig. 5) increases linearly with Ma_∞ from approximately 1 kHz at $Ma_\infty = 0.3$ to 2.58 kHz at $Ma_\infty = 0.8$. The significant peaks are marked with blue circles, and a linear fit is performed. The function with its coefficients is shown above, where the error represents the 95 % confidence bounds. When approaching transonic conditions, the schlieren snapshot reveals the formation of shocklets on the shear layer, which tend to move upstream. According to the POD mode, the periodic vortex shedding not only happens in the region toward the centerline, but also supports periodic formation of the shocklets above the shear layer. In addition, the measured schlieren flow field is more diffuse in the given FOV, and the energy is distributed slightly more across other modes. This is shown by the decrease of the percentage energy contributions $\frac{E_1}{E}$ and $\frac{E_{1:10}}{E}$. The spectra in Fig. 5 additionally show high $\widetilde{PSD}$ at multiples of the main frequency. The double frequency was found to belong to a mode present in the centerline region, where vortices from the top and bottom meet and form an alternating vortex street. Any peak at multiples of these characteristic frequencies can be attributed to the higher harmonics. It is apparent that low energy broadband contributions are found within the first ten modes as well.

When reaching supersonic outer flow (bottom row of Fig. 4), the flow starts to expand from the shrouds of the model's aft body ($x = 0,\ y \approx \pm 0.8$), which becomes visible in the schlieren snapshot. Further downstream at $x/h \approx 1.5$ the separated flows from above and below the wind tunnel model start to merge. The realignment of the flow leads to compression. Note, that both expansion and compression effects here cause a shift toward darker shading. This is due to over-deflection away from the knife edge by very strong density gradients. The spectrogram in Fig. 5 (right) reveals peaks at a characteristic frequency of approximately 5.6 kHz, which hardly changes within the range of measured supersonic Mach numbers. The dominant POD mode shows that this motion predominantly occurs at the end of the expansion fan, the shear layers, and in the region further downstream. An acoustic feedback loop between the

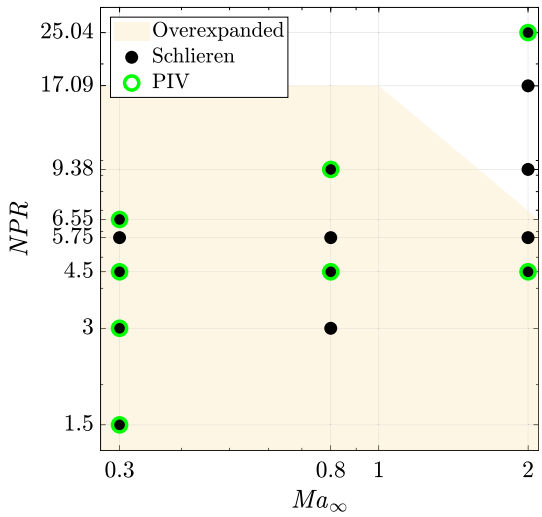


Fig. 6 Measurement matrix for the combination of nozzle and outer flow represented by *NPR* and Ma_∞, respectively

Table 2 PIV measurement and evaluation parameters for combined nozzle and outer flow measurements

	FOV1 (*xy*-plane)	FOV2 (*xz*-plane)
FOV size in px	1648/2560	2560/2160
Scaling in px/mm	19.98	30.15
Exposure time in µs	15	15
Sampling frequency in Hz	10.5	10.5
Laser pulse separation in µs	1.25 … 2.25	0.7 … 1.25
Number of double images	200	200
Window size in px	$96 \times 96 \rightarrow 12 \times 12$	$96 \times 96 \rightarrow 12 \times 12$
Window overlap in %	50	50
Vector calculation	Average correlation method (Meinhart et al. 2000)	Average correlation method (Meinhart et al. 2000)
Post-processing	Universal outlier detection (Westerweel and Scarano 2005)	Universal outlier detection (Westerweel and Scarano 2005)

shroud separation and the neck, where the sliplines converge, is likely the primary driver of the periodic motion. As upstream propagation is not possible in the supersonic region outside the sliplines, the loop is assumed to be closed via back-propagation within the slipline trajectory (Schmidt and Shepherd 2015). The $\widetilde{PSD}$ of the peaks is way lower in contrast to the characteristic peaks determined for sub-/transonic vortex shedding.

5 Interaction of nozzle and outer flow

The nozzle flow at different *NPR*s in combination with varying Ma_∞ of the outer flow is measured via PIV and schlieren, for both plug lengths subsequently. The *NPR*, as introduced earlier in Eq. 1, is hereby determined based on the control variables $p_{0,\mathrm{n}}$, $p_{0,\infty}$, and Ma_∞:

$$NPR = \frac{p_{0,\mathrm{n}}}{p_\infty} = \frac{p_{0,\mathrm{n}}}{p_{0,\infty}} \left(1 + \frac{\gamma - 1}{2} Ma_\infty^2\right)^{\frac{\gamma}{\gamma-1}}. \tag{3}$$

The heat capacity ratio γ for air is equal to 1.4. For the measurements with both nozzle and outer flow Ma_∞ is chosen to be 0.3, 0.8, and 2.0 to capture a sub-, trans-, and supersonic case each. To reach the target Mach number while maximizing the usable wind tunnel runtime, $p_{0,\infty}$ was set to 1.3 bar for $Ma_\infty = 0.3$ and 0.8, and to 2.5 bar for $Ma_\infty = 2$. For each Ma_∞ at the certain $p_{0,\infty}$, $p_{0,\mathrm{n}}$ is chosen in a way to reach desired *NPR*s (Eq. 3). The matrix of measurements taken is visualized in the scatter plot in Fig. 6. PIV measurements are executed only for selected cases. It is important to clarify, that the Ma_∞ and *NPR* shown here are the target setpoint values. The values shown in the subsequent figures of PIV and schlieren results, however, are rounded values based on wind tunnel pressure sensor data during the measurement run time. Therefore, they may differ from the target values and from one experimental run to the next. The theoretical design nozzle pressure ratio NPR_D of the nozzle is 17.09. Since $p_{0,\mathrm{n}}$ was kept below 8 bar due to material constraints, $NPR \geq NPR_\mathrm{D}$ could only be realized with supersonic outer flow. The yellow shaded area approximately marks the overexpanded regime. Note, that the actual transition happens at lower NPR when Ma_∞ approaches the supersonic regime, as the flow expands and accelerates around the aft body shrouds, increasing the effective outer Mach number and reducing the static pressure sensed by the nozzle jet (slipstream effect (Salmi and Cortright 1956)). For example, the transition for $Ma_\infty = 2$ happens around $NPR \approx 8$. This was estimated based on the flow direction change measured through PIV and the theoretical formulation for the Mach number increase described by the Prandtl–Meyer function.

It is important to mention here, that the following analysis keeps its focus on the nozzle flow combined with outer flow. For a deeper investigation of the nozzle flow itself, it is explicitly referred to the previous work by Wißmann et al. (2025).

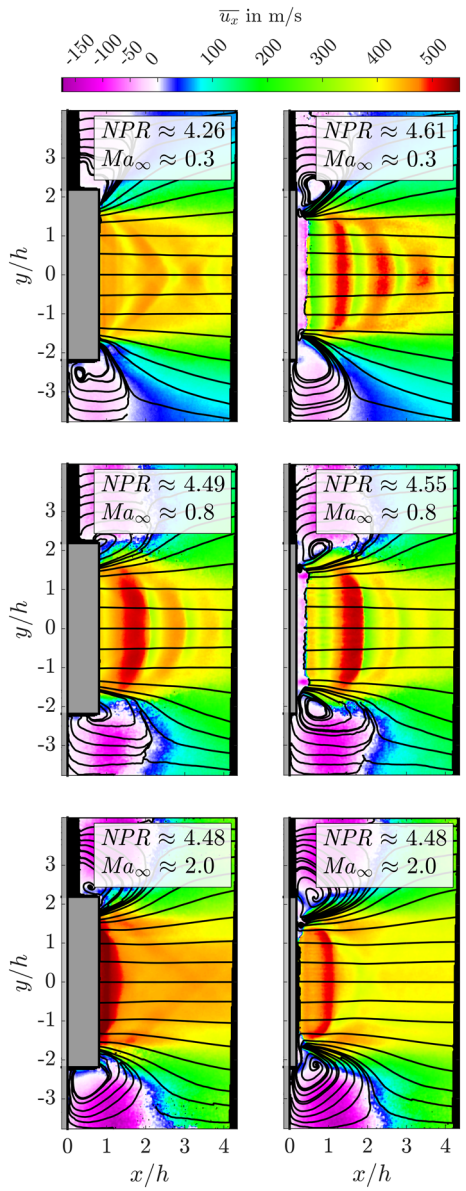


Fig. 7 Average streamwise velocity fields measured in FOV1 for *NPR*≈ 4.5, varying Ma_∞, and two different plugs A_{72} (left) and A_{24} (right)

5.1 Velocity field measurements via PIV

PIV measurements are carried out to visualize the flow field and to obtain quantitative information about the local magnitude and direction of the flow velocity. The measurement and evaluation parameters are summarized in Table 2. The parameters were optimized for obtaining a good resolution of the overall flow structure. The laser pulse separation time

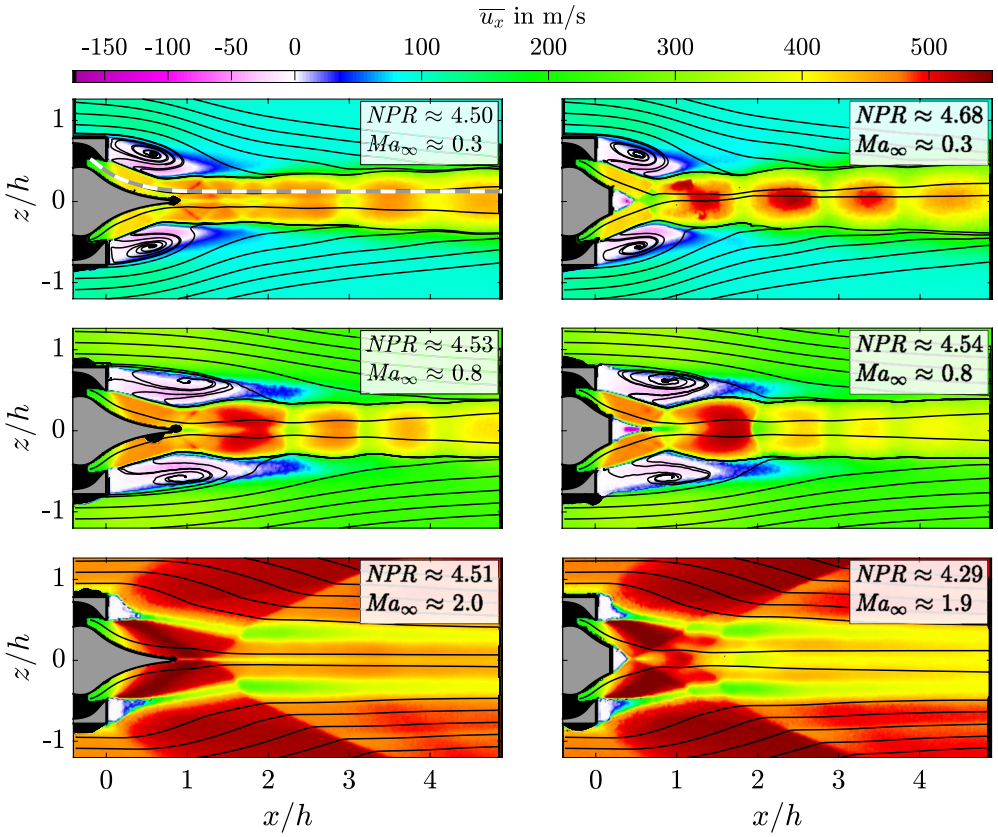


Fig. 8 Average streamwise velocity fields measured in FOV2 for $NPR \approx 4.5$, varying Ma_∞, and two different plugs A_{72} (left) and A_{24} (right)

is chosen in order to have a mean particle shift between both image frames of about 10 px to 12 px in the jet core region. At the given interrogation window size, the random error can be estimated to be around 0.07 px in an undisturbed free stream according to Scharnowski et al. (2019). However, the uncertainty may increase substantially in areas of stronger turbulence and three-dimensional flow. A limited seeding particle response time introduces an additional bias error in the regions of shock waves. The uncertainty is defined by the interrogation window size.

Measurement results for one selected $NPR \approx 4.5$ are shown in Figs. 7 and 8 for the measurement planes FOV1 and FOV2 (see Fig. 3a), respectively. The A_{72} plug is shown in the left, the A_{24} plug is shown in the right column. The average streamwise velocity $\overline{u_x}$ is computed from 200 instantaneous velocity fields and is presented via color scale in order to highlight any backflow regions. Missing and erroneous velocities are labeled in black. They are a result of no light sheet illumination or severe light scattering at the model surface. Black streamlines indicate the flow direction. The white-gray dashed line in the top left plot of Fig. 8 indicates the contour at which the velocity magnitude is extracted locally and plotted over x/h for all recorded cases (Fig. 9).

The velocity fields measured in FOV1 demonstrate a high degree of symmetry in the flow topology with respect to the centerline at $y/h = 0$. All flow fields show the existence of the expansion-compression system typical for over-expanded supersonic jet flows. The peak velocity in the jet only reaches 460 m/s for $Ma_\infty \approx 0.3$ in the A_{72} case, while it exceeds 500 m/s for A_{24}. The minimum velocity in the jet core, however, is lower. As described already in Wißmann et al. (2025), the flow expanding at the plug base shrouds and the following trailing shocks lead to this divergence. Right behind the base of the A_{24} plug a small backflow region emerges, which is measured for sub- and transonic outer flow (Fig. 7 top/middle right). For all measured cases, recirculation regions form adjacent to the nozzle throat ($|y/h| > 2$), where the backflow velocity increases with Ma_∞ and exceeds −150 m/s for supersonic outer flow. Furthermore, the recirculation regions expand further downstream as Ma_∞ increases. These observations are very similar when comparing both plug lengths. The side edges of the nozzle throats exert an influence on the two-dimensionality of the flow field. In particular, the flow from each throat also expands in the y-direction. A resulting system of expansion and compression waves produces a slight V-shaped pattern in the velocity field (see Fig. 7 top left). As the jet velocity

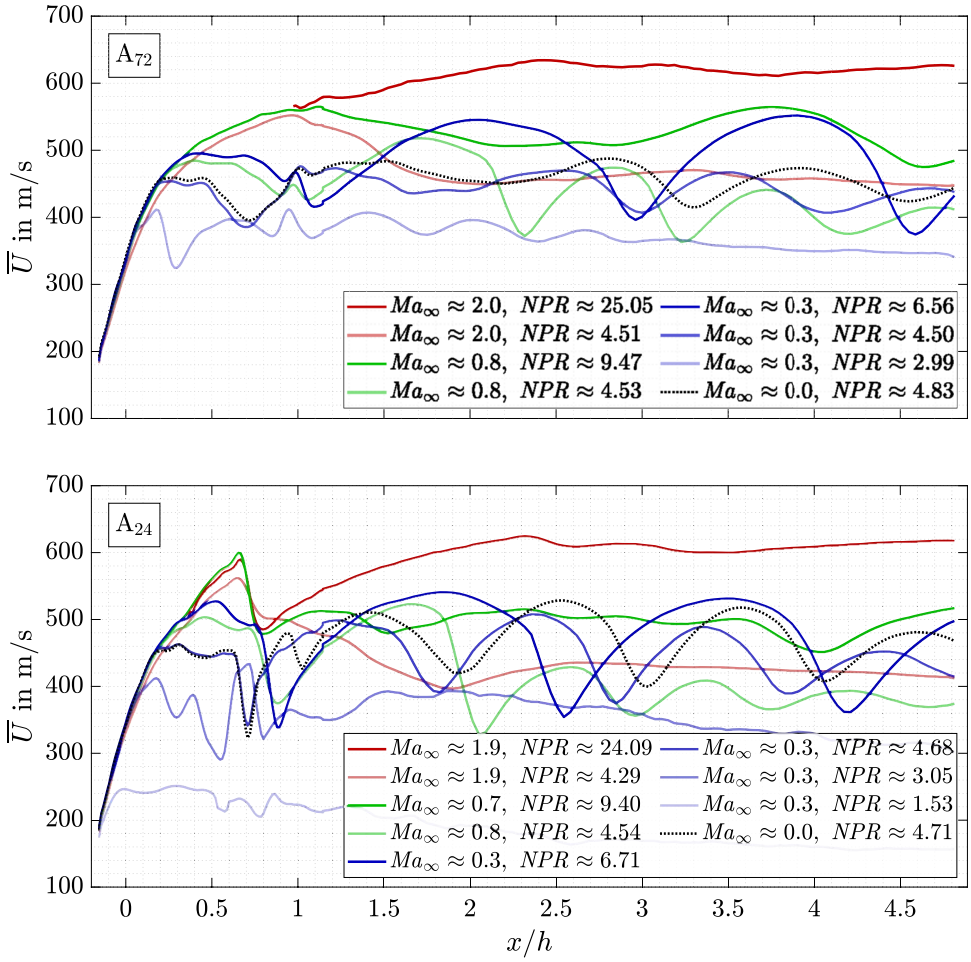


Fig. 9 Velocity profiles extracted from the contour shown in Fig. 8

increases, the pattern evolves to a U-shape, with the formation of Mach disks decelerating the air to subsonic speeds, especially in the case of the A_{24} plug (Fig. 7 middle row). In the jet flow itself, the local velocity values are quite different for both plugs and change significantly in different outer flow regimes. In general, a higher Ma_∞ leads to a reduced outer static pressure p_∞. The further reduction of the outer pressure sensed by the nozzle jet is explained by the slipstream effect, which is not accounted for in the definition of the *NPR* in Eq. 3. As a consequence, the nozzle flow expands further and reaches higher speeds, although the *NPR* is kept constant. However, stronger expansion also comes with higher velocity components in y-direction, which are unusable for the space launcher's thrust and can cause unstable flight scenarios when the local u_y tends to be unsteady.

The FOV2 results in Fig. 8 provide a view of the combined nozzle and outer flow topology with respect to the xz-plane. As expected, the flow reaches approximately sonic speed at the narrowest cross-section of the nozzle throat and accelerates to supersonic speeds further downstream. The increase in peak jet velocity with increasing outer Mach number is measured here as well. Additional insights are gained in the wake region of the upper and lower shrouds. The outer flow provokes recirculation bubbles with clockwise and counterclockwise rotation in the top and bottom half, respectively. Backflow velocities hereby reach −50 m/s, before the flow is entrained into the nozzle jet. This is observed for both sub- and transonic outer flow, while the wake region develops significantly further downstream in the latter case. The streamlines indicate the circulation regions being a source, where air enters from the sides feeding the nozzle jet. They also indicate entrainment effects, i.e. the outer flow tending to merge with the nozzle jet. This effect is observed to be stronger for lower Ma_∞ within the given FOV.

The velocity fields with the A_{72} plug reveal an additional flow expansion at the plug's tip, locally affecting the jet velocity (Fig. 8 top/middle left). In the case of A_{24} at subsonic outer flow (top right), the velocity field and streamlines in the jet core exhibit some irregularities. These are a consequence of the high unsteadiness of the flow and the PIV average correlation method, which does not demonstrate the local average velocity, but rather the most probable one. The unsteadiness is characterized by alternating

vortex shedding in the plug base region, which is seen to cause a backflow of up to −80 m/s on average. Backflow speeds of up to −150 m/s are measured in that region for the $Ma_\infty \approx 0.8$ case. At this Ma_∞, the data does not show any evidence of alternating vortices rolling in, but rather a locally stable counter-rotating vortex pair. The jump in static pressure across the trailing shocks additionally leads the air to be sucked-in toward the low pressure region close to the plug base. This is assumed to cause such high backflow speeds. The flow near the plug base wall is difficult to resolve due to scattered laser light and three-dimensional structures inducing cross-plane motion. The latter may facilitate air exchange with the outer flow. This is supported by FOV1 measurements, which indicate a lateral outflow tendency with an average velocity of $u_y \approx \pm 10$ m/s.

The velocity fields of the $Ma_\infty \approx 2$ case highlight the presence of oblique shocks, as they were sketched above in Fig. 2. For both plugs, the outer and inner realignments shocks form at $x/h \approx 0.5$, $z/h \approx \pm 0.5$. The outer shocks are a result of the outer flow vector pointing inwards after expansion at the shrouds. The flow is afterward redirected by the outer shear layers of the shroud wake, meaning the formation of compression waves that merge into shocks. The inner realignment shocks emerge from the compression through the nozzle flow being redirected/realigned by the inner shear layers of the shroud wakes. The shocks interact with the opposing inner shear layer further downstream at $x/h \approx 1.5$. The pressure increase over the shock thickens the velocity deficit region of the shroud wake locally, forming a bump in the outer shear layer. This results in oblique shocks outside, which tend to merge with the outer realignment shocks in the far field. When the plug is truncated, the flow additionally expands at the plug base shrouds, meaning a flow direction change toward the centerline. The flow being redirected shortly afterward at $x/h \approx 0.5$ results in the trailing shocks, that impinge on the inner shear layer at $x/h \approx 1$. Similar to the inner realignment shocks, they lead to a shroud wake thickening and a third oblique shock forming at the outer shear layers, which merge with the other two at $x/h \approx 2.5$ and $z/h \approx \pm 1$. This system of shock waves considerably reduces the velocity in the jet core region.

To study the variation of *NPR*, velocity profiles are extracted at a contour (gray-white line in Fig. 8 top left). The line follows the ideal plug contour with an offset of +2 mm with respect to z and continues horizontally until the end of the FOV. The profiles are plotted in Fig. 9. Different Ma_∞ are plotted with different colors, varying *NPR* is shown by different shading. Results for A_{72} and A_{24} are shown separately in the top and bottom plot, respectively. The velocity profiles for the case without outer flow, shown as dotted lines, have been already presented in Wißmann et al. (2025).

For all cases (except *NPR*≈ 1.53) the nozzle flow reaches supersonic speed right behind the throat. Starting with A_{72}, the profiles are characterized by a small peak at $x/h \approx 1$, which is due to the flow expansion around the plug's tip. This is only measured for the $Ma_\infty \approx 0.3$ cases and is slightly visible for the $Ma_\infty \approx 0.8$ case at *NPR*≈ 4.53. Further downstream the cell-like structure of the jet expresses itself in the velocity going up and down for all cases with *NPR* below the design $NPR_D \approx 17.1$ (overexpanded). Interesting to see is the comparison between both $Ma_\infty \approx 2.0$ cases, where for *NPR*≈ 4.51 the velocity drops after $x/h \approx 1$. The reason is the inner realignment shock crossing the jet flow. At $x/h \approx 1.4$ the inner realignment shock of the bottom half crosses the contour line, causing the jet velocity to decrease even further. It converges to approximately 450 m/s far downstream. For *NPR*≈ 25.05 the shock system opens up and both shocks become more horizontal, hence, not strongly affecting the jet velocity within the FOV. Another result is that the jet without outer flow (black dotted line) is faster than the flow at similar *NPR* but with subsonic outer flow. This is most prominent for $x/h > 1$. For this, it is to remembered that the *NPR* is defined based on the conditions of the outer flow surrounding the model ($x/h < 0$). Further downstream ($x/h > 0$) the outer flow gets more space, meaning a deceleration and increase in static pressure sensed by the nozzle jet. The consequence is a shrunken expansion-compression system with lower velocities in the jet core. The early jet flow ($x/h < 1$) for transonic outer flow is faster through the slipstream effect. However, a deceleration of the outer flow further downstream is observed in a similar way as for $Ma_\infty \approx 0.3$, resulting in lower jet speeds compared to the $Ma_\infty \approx 0.0$ case.

Most of what has been observed for A_{72} is also true for A_{24}. The main difference is the strong velocity drop at $x/h \approx 0.6$, which is due to the trailing shock that does not exist with such strength when the plug contour is longer. These velocity drops are emphasized in the remaining shock cell system further downstream as well. In addition, it is observed that only if the *NPR* is high enough, the flow around the plug base shrouds experiences a significant acceleration starting from $x/h \approx 0.3$. A good example for this is the comparison between both transonic cases (green curves in Fig. 9 bottom).

Table 3 Schlieren measurement parameters for combined nozzle and outer flow measurements

FOV size (x/z) in px	896/432
Scaling in px/mm	12.48
Exposure time in µs	16
Sampling frequency in kHz	58.2
Number of images	10^4

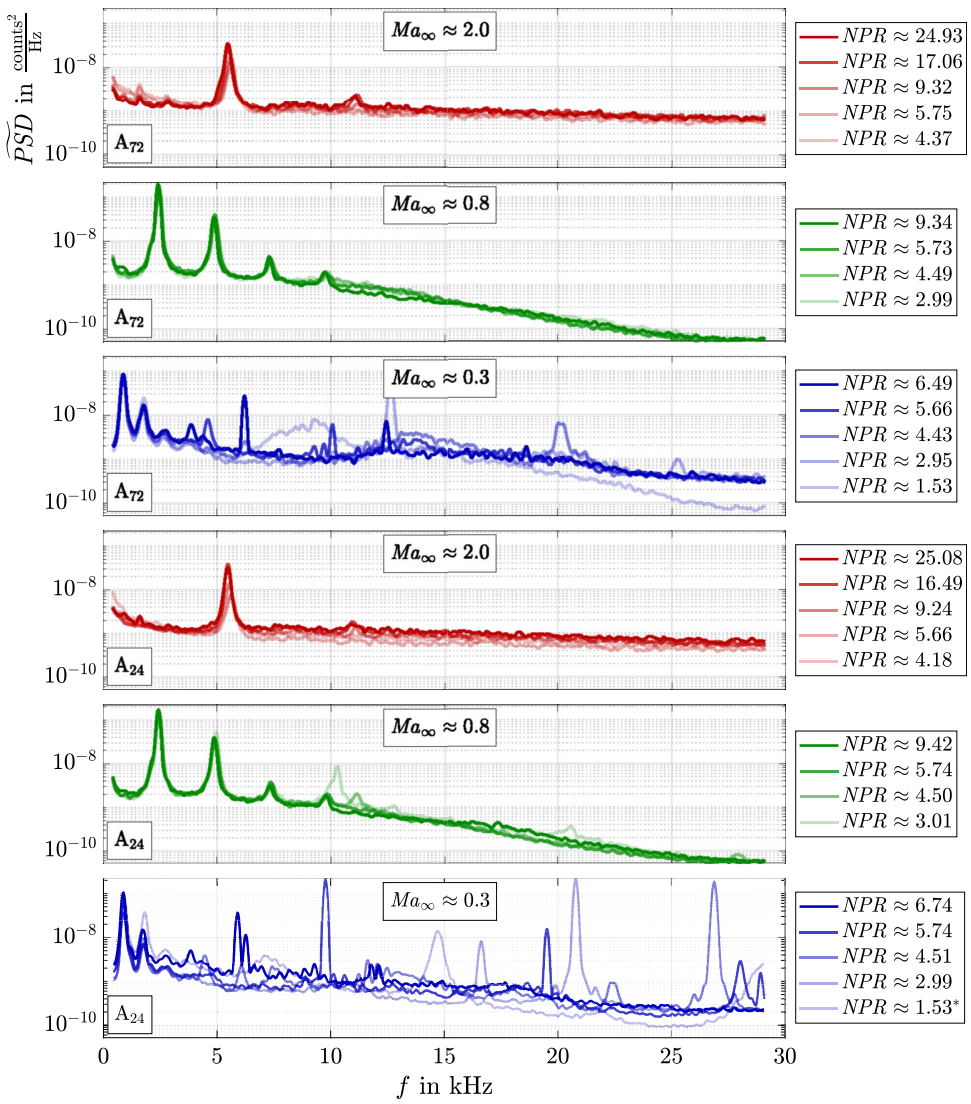


Fig. 10 Energy weighted average power spectra for all cases measured using schlieren imaging

5.2 Schlieren measurements with POD and spectral analysis

High-speed schlieren imaging helps visualizing patterns in compressible flows and identifying unsteady phenomena occurring within the jet plume, shear layer, and surrounding flow. The measurement parameters are summarized in Table 3.

POD and the energy weighted average modal spectra $\widetilde{PSD}$ (Eq. 2) are computed for all measured cases in the same way as for the outer flow characterization above. The difference is that the first sixty modes are considered for the average spectra, which goes along with the spectra computed for the nozzle flow only in Wißmann et al. (2025). The spectra are shown in the plots in Fig. 10. The top three plots belong to the longer plug A_{72}, while the bottom three belong to the short plug A_{24}. Different outer Mach numbers Ma_∞ are shown in different colors. Varying *NPR* is visualized via different color shadings. Note, that in the bottom plot the *NPR*≈ 1.53 case was unintentionally measured without tracking proper sensor data. However, the set parameters were the same as for the according case with the A_{72} plug, which is why the *NPR* is assumed to be the same, too.

With supersonic outer flow, the dominant frequency in the flow field remains largely independent of the applied *NPR*. The peak consistently lies between 5.5 kHz and 5.6 kHz across all cases, similar to measurements without nozzle flow. Increasing *NPR* slightly shifts the peak toward lower frequencies and marginally increases broadband noise at higher frequencies. Overall, the nozzle jet appears stable within the observed FOV, exhibiting no distinct periodic motion. The dominance of outer flow dynamics over nozzle behavior also holds for the $Ma_\infty \approx 0.8$ cases. This is expected, as schlieren imaging integrates over the

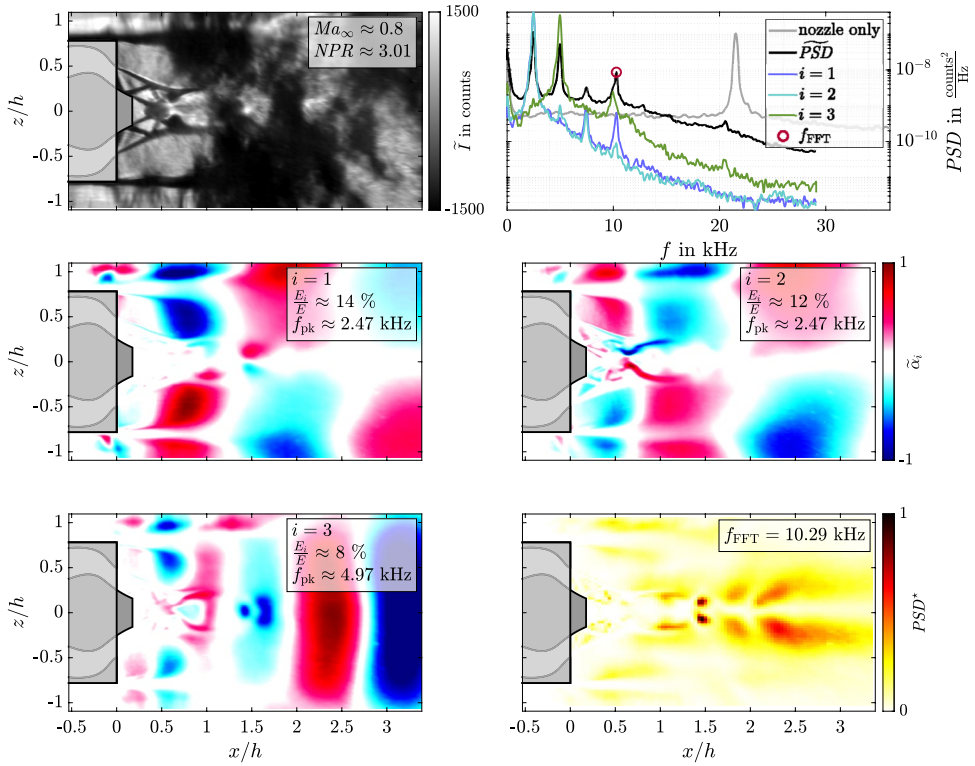


Fig. 11 Normalized schlieren intensity (top left) and four representative POD modes i (middle and bottom row) shown for the A_{24} plug for $NPR \approx 3.01$ at $Ma_\infty \approx 0.8$. The energy weighted average power spectrum $\widetilde{PSD}$, as well as the spectra of each mode are shown in the top right plot. The gray curve represents the spectrum measured at $NPR \approx 2.93$ without outer flow applied

entire span-wise y-direction, while the nozzle throat occupies only $b = 50$ mm of the 300 mm test section width. Therefore, away from the nozzle, the outer flow shows little interaction with the jet, leaving its dynamics largely unaffected. More notably, the outer flow suppresses any periodic jet modes. This aligns with the nature of screeching modes, which rely on a feedback loop between downstream-traveling Kelvin-Helmholtz (KH) instabilities and upstream-traveling acoustic waves or wave modes (Powell 1953; Tam and Ahuja 1990; Shen and Tam 2002). At local sonic or supersonic outer Mach numbers, this loop is disrupted, preventing excitation of KH instabilities and thus inhibiting screech.

Special cases arise at low NPR and $Ma_\infty \approx 0.8$ for the truncated plug. At $NPR \approx 3.01$, a pronounced peak at 10.29 kHz is observed. This case is examined in more detail in Fig. 11, where a snapshot of the normalized schlieren intensity $\widetilde{I}$ is shown in the top left. In addition, the first three POD modes are illustrated below including their percentage energy contribution. In the top right the spectrum of each shown mode is plotted, as well as the energy weighted average $\widetilde{PSD}$ from Fig. 10. The average spectrum of a similar case but without outer flow (Wißmann et al. 2025) is presented in gray. The first two POD modes exhibit asymmetric patterns slightly offset from each other, which is characteristic for alternating vortex shedding from the outer flow with downstream-traveling structures. The second spectral peak, at double the frequency, corresponds to the third, symmetric mode, which primarily represents the downstream vortex street. The 10.29 kHz component could not be clearly decomposed by POD and appears entangled with the first mode, which occurs at approximately one fourth of its frequency. To better localize this feature, a spatially resolved FFT was applied to the schlieren data, and the normalized spectral power density $PSD^\star$ at $f_{\mathrm{FFT}} = 10.29$ kHz is shown in the bottom right of Fig. 11. The frequency appears in the jet core near $x/h \approx 1.5$ and indicates oscillatory motion of the jet tail extending downstream. The physical origin remains uncertain, since screech requires upstream feedback, which was found to not be given for other cases at $Ma_\infty \approx 0.8$. However, PIV measurements reveal a long subsonic or backflow region in the shroud wake (see Fig. 8 second row), potentially enabling upstream-traveling acoustic waves to reach the nozzle lip. These waves likely originate at shock cell boundaries, which are more contracted at lower NPRs and may lie within the subsonic wake region. Notably, no such peak appears in the A_{72} measurements, suggesting the stronger plug truncation and resulting bluff body wake also playing a role. A key difference is the position and intensity of the trailing shocks, which may interact with KH instabilities in the shear layer and act as an additional acoustic source.

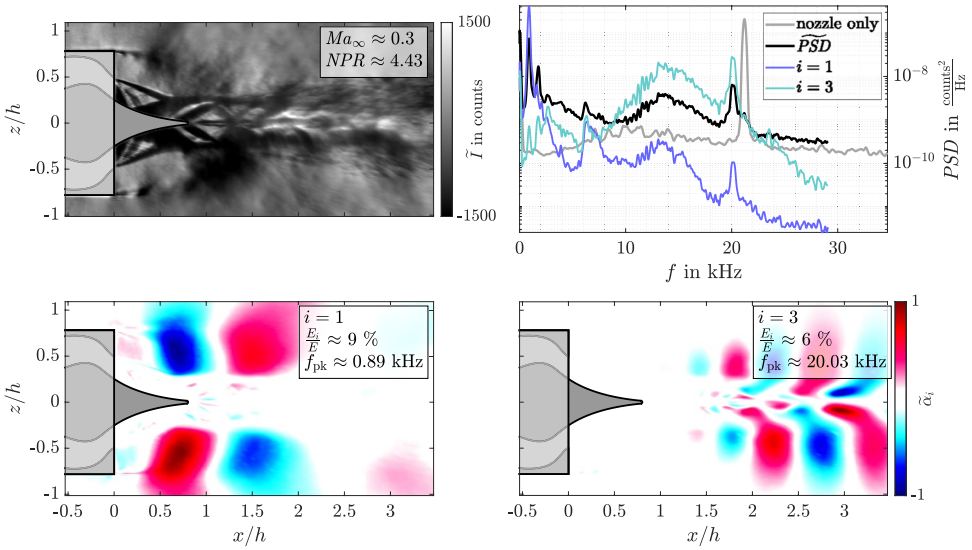


Fig. 12 Normalized schlieren intensity (top left) and two representative POD modes i (bottom row) shown for the A_{72} plug for $NPR \approx 4.43$ at $Ma_\infty \approx 0.3$. The energy weighted average power spectrum $\widetilde{PSD}$, as well as the spectra of both modes are shown in the top right plot. The gray curve represents the spectrum measured at $NPR \approx 4.47$ without outer flow applied

At subsonic outer flow, the spectra (Fig. 10 blue curves) reveal a variety of characteristic frequencies with heavy dependence on the *NPR*. This has been recorded for measurements without outer flow as well (Wißmann et al. 2025). Assuming that the periodic motions originate from a jet screeching phenomenon, it makes sense that this is observed when the outer flow is globally subsonic. Without outer flow, the dominant screeching frequency f_s can be predicted using the model by Powell (1953, 1953):

$$f_s = \frac{U_c}{s(1 + Ma_c)} \,. \tag{4}$$

The shock cell spacing s is seen to increase with increasing *NPR*, causing a reduction in screeching frequency. The convection velocity U_c and convection Mach number Ma_c are commonly estimated based on the velocity inside the jet U_j. For rectangular jets Tam and Reddy (1996) proposed the following relation:

$$U_c \approx 0.55 \cdot U_j \,. \tag{5}$$

However, for in-flight conditions, i.e. with an outer flow of certain Mach number Ma_∞ and velocity U_∞ the dominant screech tone changes. This is due to the fact that the convection velocity U_c and effective speed of the acoustic waves traveling upstream change. The increase of U_c has firstly been defined by Bryce and Pinker (1977):

$$U_c \Rightarrow 0.55 \cdot (U_j - U_\infty) + U_\infty = 0.55 \cdot U_j + 0.45 \cdot U_\infty \,. \tag{6}$$

The acoustic waves traveling outside and closing the feedback loop are facing against the outer flow. Bryce and Pinker (1977) suggested the back-propagation velocity is the ambient speed of sound c_∞ minus the outer flow velocity:

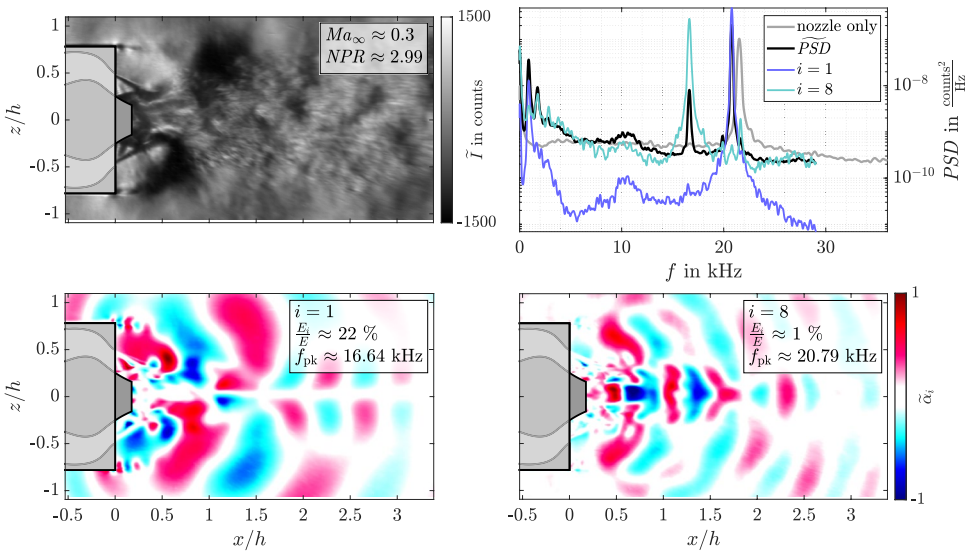


Fig. 13 Normalized schlieren intensity (top left) and two representative POD modes i (bottom row) shown for the A_{24} plug for $NPR \approx 2.99$ at $Ma_\infty \approx 0.3$. The energy weighted average power spectrum $\widetilde{PSD}$, as well as the spectra of both modes are shown in the top right plot. The gray curve represents the spectrum measured at $NPR \approx 2.93$ without outer flow applied

$$c_\infty \Rightarrow c_\infty - U_\infty \,. \tag{7}$$

Implementing these adaptations in Eq. 4, the in-flight screech tone prediction reads as

$$f_{s,\infty} = \frac{U_c}{s(1+\frac{Ma_c}{1-Ma_\infty})} = \frac{U_c}{s(1+\frac{U_c}{c_\infty - U_\infty})} \,. \tag{8}$$

Ultimately, the screeching frequency should decrease with higher outer Mach numbers and converges to Eq. 4 for $U_\infty \rightarrow 0$. The frequency could finally be expressed as normalized Strouhal number Sr according to

$$Sr_{s,\infty} = \frac{f_{s,\infty} \cdot h}{U_j} \,, \tag{9}$$

whereas in this paper the frequency unit is kept in absolute numbers.

The case shown in Fig. 12 is representative for most of the measurements with subsonic outer flow. Here, the amplified screeching mode ($i = 3$) with its characteristic frequency of 20.03 kHz is shown, alongside the outer flow mode ($i = 1$). The screech mode is most dominant at $x/h \approx 3$. The spectrum of the nozzle flow shows a peak that is slightly shifted toward higher frequencies (21.2 kHz). This observation is consistent with Eq. 8. The $NPR \approx 6.49$ case was found to deviate from these observations in a sense that the screech frequency increased when comparing subsonic outer flow with no outer flow. One factor hereby is the way how the NPR is defined (Eq. 3). In the PIV measurements, it was shown that the deceleration of the subsonic outer flow behind the model's aft body leads to the nozzle jet facing against a higher static pressure. Ultimately, the jet speed is reduced (Fig. 9). On top of that, the shock cell length s shrinks, meaning that f_s has to increase according to Eq. 4 or Eq. 8. Another factor could be the backflow region in the shroud wake, which locally accelerates the acoustic waves as a feedback mechanism, further increasing the screeching frequency. It remains unclear why just at this specific NPR the frequency is shifted to higher values. It is suspected that the outer flow not only alters the frequency, but additionally influences the mode staging behavior (Davies and Oldfield 1962), i.e. affecting which screech mode becomes dominant.

All those observations are made for the truncated plug in a similar way as well. The main addition is the flow unsteadiness behind the plug base. When increasing the NPR, the flow in the plug wake region transitions from a strong oscillatory motion to two locally stable counter-rotating vortices. The same has been measured without any outer flow (Wißmann et al. 2025). The oscillation frequency is about 26.9 kHz for $NPR \approx 4.51$ and decreases to 20.8 kHz or 14.7 kHz for $NPR \approx 2.99$ or 1.53, respectively. Two POD modes and their spectra are shown for the $NPR \approx 2.99$ case in Fig. 13. The first one describes the oscillatory motion and the spherical propagation of acoustic waves from the shear layers at $x/h \approx 0.4$. From the spectrum, it becomes clear that the outer flow dynamics are included in this mode, too. A second spectral peak at 16.6 kHz appears in the eighth mode, localized in the jet core near $x/h \approx 0.5$ with symmetric downstream-propagating waves. The origin of this mode remains unclear, as it is absent without outer flow.

6 Summary and conclusions

In a controlled wind tunnel setting the flow field of a linear plug nozzle with two truncation lengths (72 % and 24 % of the full-length) is investigated by means of PIV and high-speed schlieren imaging. The jet plume was studied at a variety of NPR in combination with outer Mach numbers in the sub-, trans-, and supersonic regime. The outcome of the study is concluded in the following, referring back to the research questions stated in section 2:

- The nozzle flow expands to supersonic speed downstream of the throat and is characterized by a system of expansion and compression waves, also in the span-wise xy-plane. Backflow and subsonic regions emerge adjacent to the nozzle throats, and in the wake of the aft body shrouds and plug base. The velocity magnitudes in the jet core and in these backflow regions depend on both NPR and Ma_∞. The slipstream effect, where the trans-/supersonic outer flow accelerates around the shroud edges and reduces the local static pressure sensed by the jet, leads to stronger expansion and to higher velocities inside the jet close to the throats. Plug truncation comes with an additional flow acceleration followed by trailing shocks, which interact with the inner shear layers of the shroud wakes. When the outer flow is supersonic, inner and outer realignment shocks form at the inner and outer shear layers of the shroud wakes. The system of compression shocks leads to a significant reduction of the flow velocity in the jet core region. The NPR and Ma_∞ determine the angle of those shocks and therefore the location of the deceleration effects.
- The base region behind the truncated plug is characterized by either a highly unsteady alternating vortex shedding mode, or by two counter-rotating vortices. Both phenomena lead to subsonic backflow of different magnitude. The effective NPR determines which phenomenon is occurring. At trans- and supersonic outer flow the aerodynamic phenomena from the nozzle jet, namely jet screeching and vortex shedding modes, are almost entirely suppressed. The possibility for jet screeching at transonic flight velocity is suspected to only be

given when the subsonic region in the aft body shroud wake spreads across the acoustic sources responsible for screeching (shock cell boundaries). According to this, a more aerodynamic aft body shape (boat-tail) could possibly suppress harmful aeroacoustics of a future space launcher, alongside minimizing the base drag, reducing the total weight, and increasing the structural durability. At subsonic outer flow, the nozzle jet is characterized by a multitude of periodic modes. The screeching frequency is seen to slightly decrease with respect to the frequencies measured without outer flow, which is in agreement with theoretical formulations. However, plenty of measurement cases show deviations from the theory, which, on the one hand, are suspected to be a result of the outer flow affecting the mode staging behavior. On the other hand, the shroud wake region covers a range of subsonic flow velocities, as well as backflow regions, through which the acoustic feedback might locally experience accelerations and decelerations. The dominant frequency is therefore difficult to predict.

In general, the definition of the *NPR* was seen to be rather vague when dealing with in-flight scenarios. At any Ma_∞ the outer flow velocity and static pressure locally changes with downstream direction. Consequently, the *NPR* experienced by the jet at any streamwise location can deviate from the theoretically defined *NPR*. The jet speed and aeroacoustic footprint are therefore prone to deviations as well. This leads to situations where the nozzle jet expansion system locally behaves considerably different at different Ma_∞, although the *NPR* is similar.

Open questions remain regarding the scalability of the results presented in this study. Although until now there is no full-scale commercial space launcher operating with a plug nozzle as a thrust generator, the results could contribute to make expensive near-reality tests more and more predictable. However, when firing a hot exhaust gas, thermo-acoustic instabilities might affect the jet plume's dynamic behavior, which was not accounted for in this work. In addition, full-scale models of linear aerospike engines[2] would have multiple small combustion chambers (nozzle cluster) instead of two throats as a long slit. While this enables thrust vector control via differential throttling, the aerodynamic implications of such are poorly researched. For this reason, future work will focus on wind tunnel investigations of the flow of a clustered linear aerospike nozzle at various in-flight steering scenarios.

Supplementary Information The online version contains supplementary material available at https://doi.org/10.1007/s00348-025-04098-7.

[2] A prominent candidate is the Rocketdyne XRS-2200 developed for the Lockheed Martin X-33 program (D'Agostino et al. 2001).

Acknowledgements The financial support of the German Research Foundation (DFG) under the Grant number 464275368 is gratefully acknowledged by the authors.

Author contributions Sven Scharnowski conceived the presented research objectives. Paul Wißmann performed the measurements, processed the experimental data, performed the analysis, drafted the manuscript and designed the figures. Sven Scharnowski and Christian J. Kähler were involved in planning and supervising the work, and aided in interpreting the results. All authors discussed the results and commented on the manuscript.

Funding Open Access funding enabled and organized by Projekt DEAL.

Data availability Exemplary schlieren videos and PIV raw images, as well as nozzle geometry data are provided within the supplementary files.

Declarations

Conflict of interest The authors declare no conflict of interest.

Open Access This article is licensed under a Creative Commons Attribution 4.0 International License, which permits use, sharing, adaptation, distribution and reproduction in any medium or format, as long as you give appropriate credit to the original author(s) and the source, provide a link to the Creative Commons licence, and indicate if changes were made. The images or other third party material in this article are included in the article's Creative Commons licence, unless indicated otherwise in a credit line to the material. If material is not included in the article's Creative Commons licence and your intended use is not permitted by statutory regulation or exceeds the permitted use, you will need to obtain permission directly from the copyright holder. To view a copy of this licence, visit http://creativecommons.org/licenses/by/4.0/.

References

Angelino G (1964) Approximate method for plug nozzle design. AIAA J 2(10):1834–1835. https://doi.org/10.2514/3.2682

Arnold GA (1954) Jet-propulsion nozzle for use at supersonic jet velocities. Google Patents. US Patent 2683962

Besnard E, Garvey J, Holleman T, Mueller T, Chen HH, Chen H-P (2002) Student development and test of a gimbaled annular aerospike engine. In: 38th AIAA/ASME/SAE/ASEE joint propulsion conference & exhibit. https://doi.org/10.2514/6.2002-4184

Bharathwaj M, Krishna TV, Nanda SR, Karthick S, Sugarno MI (2024) On the unsteady flow dynamics of a planar-plug nozzle with a semi-extended cowl. Phys Fluids 36(11):116105. https://doi.org/10.1063/5.0237453

Bolgar I, Scharnowski S, Kähler CJ (2018) The effect of the mach number on a turbulent backward-facing step flow. Flow Turbul Combust 101:653–680. https://doi.org/10.1007/s10494-018-9921-7

Bryce W, Pinker R (1977) The noise from unheated supersonic jets in simulated flight. In: 4th Aeroacoustics conference, p 1327. https://doi.org/10.2514/6.1977-1327

Bui T, Murray J, Rogers C, Bartel S, Cesaroni A, Dennett M (2005) Flight research of an aerospike nozzle using high power solid rockets. In: 41st AIAA/ASME/SAE/ASEE joint propulsion conference & exhibit, p 3797. https://doi.org/10.2514/6.2005-3797

Burry RV, Iacobellis SF, Larson VR (1967) Liquid propellant rocket engines - their status and future. J Spacecr Rocket 4(12):1569–1580. https://doi.org/10.2514/3.29135

Chutkey K, Viji M, Verma SB (2018) Interaction of external flow with linear cluster plug nozzle jet. Shock Waves 28:1207–1221. https://doi.org/10.1007/s00193-018-0849-6

Corda S, Bradford N, Moes T, Cox T, Monaghan R, Voelker L, Corpening G, Larson R (1998) Flight testing the linear aerospike SR-71 experiment (LASRE). In: 30th anniversary symposium of the society of flight test engineers, Inc. NASA Dryden Flight Research Center

D'Agostino MG, Lee YC, Wang T-S, Turner J (2001) X-33 XRS-2200 linear aerospike engine sea level plume radiation. In: 26th JANNAF exhaust plume technology subcommittee meeting

Davies M, Oldfield D (1962) Tones from a choked axisymmetric jet. II. the self excited loop and mode of oscillation. Acta Acust Acust 12(4):267–277

Geron M, Paciorri R, Nasuti F, Sabetta F, Martelli E (2005) Transition between open and closed wake in 3d linear aerospike nozzles. In: 41st AIAA/ASME/SAE/ASEE joint propulsion conference & exhibit, p 4308. https://doi.org/10.2514/6.2005-4308

Golliard T, Mihaescu M (2024) Computational aeroacoustics for a cold, non-ideally expanded aerospike nozzle. J Turbomach 146(2):021003. https://doi.org/10.1115/1.4063877

Hagemann G, Immich H, Van Nguyen T, Dumnov GE (1998) Advanced rocket nozzles. J Propul Power 14(5):620–634. https://doi.org/10.2514/2.5354

Hagemann G, Immich H, Terhardt M (1998) Flow phenomena in advanced rocket nozzles-the plug nozzle. In: 34th AIAA/ASME/SAE/ASEE joint propulsion conference and exhibit, p 3522. https://doi.org/10.2514/6.1998-3522

Immich H, Nasuti F, Onofri M, Caporicci M (1998) Experimental and numerical analysis of linear plug nozzles. In: 8th AIAA international space planes and hypersonic systems and technologies conference, p 1603. https://doi.org/10.2514/6.1998-1603

Karthikeyan N, Verma S, Venkatakrishnan L (2009) Experimental investigation of the acoustics of an annular aerospike nozzle flow. In: 15th AIAA/CEAS aeroacoustics conference (30th AIAA aeroacoustics conference), p 3375. https://doi.org/10.2514/6.2009-3375

Manski D, Hagemann G (1996) Influence of rocket design parameters on engine nozzle efficiencies. J Propul Power 12(1):41–47. https://doi.org/10.2514/3.23988

Meinhart CD, Wereley ST, Santiago JG (2000) A PIV algorithm for estimating time-averaged velocity fields. J Fluids Eng 122(2):285–289. https://doi.org/10.1115/1.483256

Nasuti F, Onofri M (2001) Analysis of in-flight behavior of truncated plug nozzles. J Propul Power 17(4):809–817. https://doi.org/10.2514/2.5837

Nave L, Coffey G (1973) Sea level side loads in high-area-ratio rocket engines. In: 9th Propulsion Conference, p 1284. https://doi.org/10.2514/6.1973-1284

Onofri M, Calabro M, Hagemann G, Immich H, Sacher P, Nasuti F, Reijasse P (2002) Plug nozzles: summary of flow features and engine performance-overview of RTO/AVT WG 10 subgroup 1. In: 40th AIAA aerospace sciences meeting & exhibit, p 584. https://doi.org/10.2514/6.2002-584

Powell A (1953) On the mechanism of choked jet noise. Proc Phys Soc 66(12):1039. https://doi.org/10.1088/0370-1301/66/12/306

Powell A (1953) On the noise emanating from a two-dimensional jet above the critical pressure. Aeronaut Q 4(2):103–122. https://doi.org/10.1017/S0001925900000822

Powis AT, Brunet RJ, Lynch JP, Honnery DR, Soria J, Edgington-Mitchell D (2016) Impingement tones and associated shock instabilities in supersonic plug nozzle flows. AIAA J 54(9):2843–2851. https://doi.org/10.2514/1.J054429

Raffel M, Willert CE, Scarano F, Kähler CJ, Wereley ST, Kompenhans J (2018) Particle Image Velocimetry: a Practical Guide, 3rd edn. Springer, Cham, Switzerland. https://doi.org/10.1007/978-3-319-68852-7

Ragni D, Schrijer F, Van Oudheusden B, Scarano F (2011) Particle tracer response across shocks measured by PIV. Exp Fluids 50:53–64. https://doi.org/10.1007/s00348-010-0892-2

Ruf J, McConaughey P (1997) The plume physics behind aerospike nozzle altitude compensation and slipstream effect. In: 33rd joint propulsion conference and exhibit, p 3218. https://doi.org/10.2514/6.1997-3218

Salmi RJ, Cortright E (1956) Effects of external stream flow and afterbody variations on the performance of a plug nozzle at high subsonic speeds. RM E56Flla, National Advisory Committee for Aeronautics

Scharnowski S, Kähler CJ (2021) Investigation of the base flow of a generic space launcher with dual-bell nozzle. CEAS Space J 13(2):197–216. https://doi.org/10.1007/s12567-020-00333-5

Scharnowski S, Bolgar I, Kähler CJ (2017) Characterization of turbulent structures in a transonic backward-facing step flow. Flow Turbul Combust 98:947–967. https://doi.org/10.1007/s10494-016-9792-8

Scharnowski S, Bross M, Kähler CJ (2019) Accurate turbulence level estimations using PIV/PTV. Exp Fluids 60:1–12. https://doi.org/10.1007/s00348-018-2646-5

Scharnowski S, Bolgar I, Kähler CJ (2016) Investigation of a generic space launcher wake in sub-, trans- and supersonic conditions. In: International workshop on non-intrusive optical flow diagnostics

Schmidt BE, Shepherd JE (2015) Oscillations in cylinder wakes at mach 4. J Fluid Mech 785:3. https://doi.org/10.1017/jfm.2015.668

Shen H, Tam CK (2002) Three-dimensional numerical simulation of the jet screech phenomenon. AIAA J 40(1):33–41. https://doi.org/10.2514/2.1638

Tam CK, Ahuja K (1990) Theoretical model of discrete tone generation by impinging jets. J Fluid Mech 214:67–87. https://doi.org/10.1017/S0022112090000052

Tam CK, Reddy N (1996) Prediction method for broadband shock-associated noise from supersonic rectangular jets. J Aircr 33(2):298–303. https://doi.org/10.2514/3.46937

Tobias JR, Agrawal AK (2023) Flow development in radial plane of rotating detonation engine integrated with aerospike. J Propul Power 39(3):318–330. https://doi.org/10.2514/1.B38874

Tomita T, Tamura H, Takahashi M (1996) An experimental evaluation of plug nozzle flow field. In: 32nd joint propulsion conference and exhibit, p 2632. https://doi.org/10.2514/6.1996-2632

Verma SB (2009) Performance characteristics of an annular conical aerospike nozzle with freestream effect. J Propul Power 25(3):783–791. https://doi.org/10.2514/1.40302

Welch P (1967) The use of fast fourier transform for the estimation of power spectra: A method based on time averaging over short, modified periodograms. IEEE Trans Audio Electroacoust 15(2):70–73. https://doi.org/10.1109/TAU.1967.1161901

Westerweel J, Scarano F (2005) Universal outlier detection for PIV data. Exp Fluids 39:1096–1100. https://doi.org/10.1007/s00348-005-0016-6

Wisse MEN, Bannink WJ (2001) Half model restrictions for linear plug nozzle testing. AIAA J 39(11):2148–2157. https://doi.org/10.2514/2.1211

Wisse MEN, Bannink WJ (2003) Trailing-edge cavity afterbodies for linear plug nozzle engines. AIAA J 41(9):1715–1721. https://doi.org/10.2514/2.7317

Wißmann P, Kähler CJ, Scharnowski S (2024) PIV and schlieren measurements of a linear plug nozzle jet interacting with external flow.

In: 21st international symposium on applications of laser and imaging techniques to fluid mechanics. https://doi.org/10.55037/lxlaser.21st.18

Wißmann P, Kähler CJ, Scharnowski S (2025) On the dynamics of linear plug nozzle flows under various operating conditions. AIAA J.https://doi.org/10.2514/1.J064767

Zaman KQ, Fagan AF, Bridges JE, Heberling B (2022) Flow and noise from supersonic plug nozzles. In: 28th AIAA/CEAS aeroacoustics 2022 conference, p 2828. https://doi.org/10.2514/6.2022-2828

Zaman KQ, Korth JH, Fagan AF, Bridges JE (2024) Study of a plug nozzle for supersonic aircraft concepts. In: 30th AIAA/CEAS aeroacoustics conference, p 3035. https://doi.org/10.2514/6.2024-3035

Zigunov F (2024) POD - Proper Orthogonal Decomposition (Wrapper). MATLAB Central File Exchange. https://www.mathworks.com/matlabcentral/fileexchange/71421-pod-proper-orthogonal-decomposition-wrapper

Publisher's Note Springer Nature remains neutral with regard to jurisdictional claims in published maps and institutional affiliations.